ACS NANO

www.acsnano.org

ARTICLE

Plasmon-Enhanced Resonant Photoemission Using Atomically Thick Dielectric Coatings

Xiao Xiong,[#] Yang Zhou,[#] Yi Luo, Xiang Li, Michel Bosman, Lay Kee Ang, Peng Zhang,* and Lin Wu*

Cite This: *ACS Nano* 2020, 14, 8806–8815

Read Online

ACCESS | Metrics & More | Article Recommendations | Supporting Information

ABSTRACT: **By proposing an atomically thick dielectric coating on a metal nanoemitter, we theoretically show that the optical field tunneling of ultrafast-laser-induced photoemission can occur at an ultralow incident field strength of 0.03 V/nm. This coating strongly confines plasmonic fields and provides secondary field enhancement beyond the geometrical plasmon field enhancement effect, which can substantially reduce the barrier and enable more efficient photoemission. We numerically demonstrate that a 1 nm thick layer of SiO_2 around a Au-nanopyramid will enhance the resonant photoemission current density by 2 orders of magnitude, where the transition from multiphoton absorption to optical field tunneling is accessed at an incident laser intensity at least 10 times lower than that of the bare nanoemitter. The effects of the coating properties such as refractive index, thickness, and geometrical settings are studied, and tunable photoemission is numerically demonstrated by using different ultrafast lasers. Our approach can also directly be extended to nonmetal emitters, to—for example—2D material coatings, and to plasmon-induced hot carrier generation.**

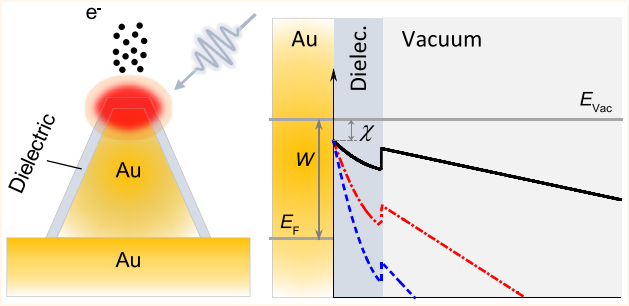

KEYWORDS: *resonant photoemission, atomically thick dielectric coating, plasmon field confinement, ultrafast lasers, multiphoton absorption, optical field tunneling*

Photoelectron emission, or photoemission, from a nanotip driven by an ultrafast laser offers an attractive route to generate high brightness, low emittance, and spatiotemporally coherent electron bunches,[1−6] which are central to time-resolved electron microscopy,[7] free-electron lasers,[8] carrier-envelope-phase detection,[9] and novel nanoelectronic devices.[10−12] Despite extensive research exploring efficient multiphoton absorption at low laser intensities or optical field tunneling at high laser intensities,[8,13−15] the use of photoemission from nanotips is still limited by its low emission current and low quantum efficiency. It has been proposed to enhance the photoemission by adding a strong dc bias,[8,14,16−21] but the optical field enhancement near the apex of the nanotip is still relatively low, typically only 10 times,[4,16] making the optical field tunneling accessible only at high incident laser fields, *e.g.*, 1.22 V/nm.[9]

Metal nanoparticles can offer significantly high optical field enhancements due to localized surface plasmon resonances,[22] thus enabling strong-field photoemission at resonant wavelengths.[23−26] For example, ultrafast generation of electrons from tailored metal nanoparticles has been demonstrated, and the role of plasmon resonant field enhancement in this process was unravelled by comparing resonant and off-resonant particles.[23] Strong-field, carrier-envelope-phase-sensitive photoemission from arrays of metal nanoparticles has also been demonstrated, where the influence of the nanoparticle geometry and the plasmon resonance on the phase-sensitive response was studied.[25] While highly nonlinear optical processes are typically achieved with ultrafast lasers, a localized three-photon photoemission was however demonstrated under continuous-wave illumination at sub-MW/cm^2 from gold nanostars with a feature size of <5 nm, where the local intensity enhancement exceeds 1000.[27] Such plasmon-enhanced fields were found to drastically increase the photon-to-current conversion efficiency by over 2 orders of magnitude.[28]

In this work, we propose to coat the metal nanoemitters with an atomically thick dielectric to further enhance the plasmonic photoemission, where optical field tunneling can be accessed at a significantly reduced incident laser intensity. The physics behind this effect lies in the considerably enhanced plasmon resonant fields highly confined within the dielectric coating (in addition

Received: April 23, 2020
Accepted: June 22, 2020
Published: June 22, 2020

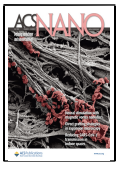

https://dx.doi.org/10.1021/acsnano.0c03406
ACS Nano 2020, 14, 8806–8815

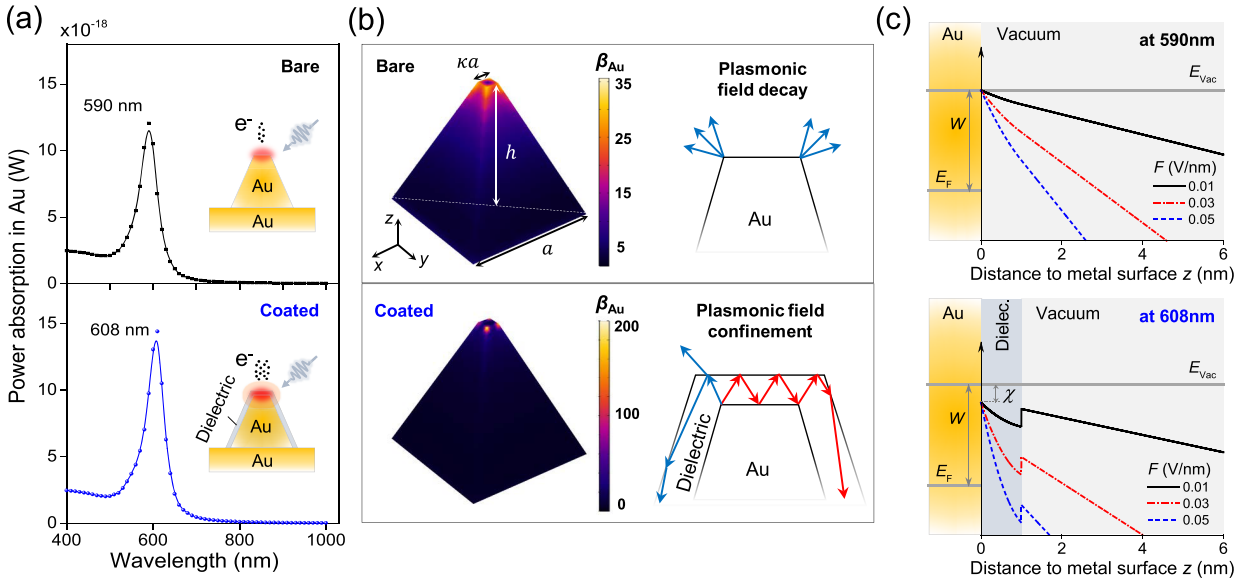

Figure 1. Resonant photoemission. (a) Schematic of the resonant photoemission from either bare or coated Au-nanopyramid field emitters (insets) with their simulated plasmon resonances. (b) Corresponding simulated resonant field enhancements β_{Au} at the Au surface, with insets illustrating the mechanism of the plasmonic field confinement providing a secondary field enhancement. In the simulation, the nanopyramid has fixed side length a = 40 nm, height h = 40 nm, and aspect ratio κ = 0.1. It is either bare or coated with a dielectric layer with thickness d = 1 nm and refractive index n = 1.5. (c) Potential profiles of the tunneling barriers induced by different field strengths F of the incident laser.

to the geometrical plasmon field enhancement) and the lowered tunneling barrier due to the electron affinity. We perform optical simulations and employ a quantum photoemission model to investigate the photoemission processes under the plasmon resonant conditions on both bare and coated Au-nanopyramid field emitters. The proposed mechanism is independent of the geometry of the metal nanoemitter, and practically the coating could protect the metal nanoemitters from corrosion or metal-atom migration under intense optical fields.[29] The ideas presented in this work may result in the fabrication of strong-field photoemitters with higher yields and longer lifetimes.

RESULTS AND DISCUSSIONS

The first step of our study is the design of an efficient plasmonic photoemitter supporting antenna mode[30] by full-wave optical simulations (see Methods),[31−33] so that the incident optical energy could be maximally concentrated to the tip of the emitter. Figure 1a illustrates the schematics of the bare and coated Au-nanopyramid field emitters sitting on a Au substrate (insets) and their plasmon resonances excited by a z-polarized light from the side. Here, the choice of substrate and incident polarization is to assist the efficient excitation of the antenna mode (see Supporting Information S1). The nanopyramid emitter has a side length of a at the bottom surface or κa at the top surface and height h, either bare in a vacuum or coated with a thin dielectric layer of thickness d and refractive index n. The geometrical settings of the nanopyramid emitters (a, κ, and h) are used to design the resonant wavelength of the antenna mode (see Supporting Information S2).

Resonant Photoemission. For a typical photoemitter with $a = h$ = 40 nm and κ = 0.1, under the illumination of z-polarized light from the side, we observe the antenna mode at 590 nm for the bare photoemitter or at 608 nm for the coated photoemitter (d = 1 nm, n = 1.5). Though occurring at similar resonant wavelengths, the plasmon field enhancement and the underlying microscopic physics differ drastically. As shown in Figure 1b, for the bare Au-nanopyramid (top), a typical plasmonic nanostructure, the enhanced plasmonic field concentrates at the sharp corners of the Au (maximum field enhancement β_{Au} = 35), and its magnitude exponentially decays going into the vacuum, dying out at a distance of <10 nm. In contrast, for the coated case (bottom), the dielectric coating with a refractive index n creates an interface with the vacuum. This interface helps to reflect and confine the plasmonic fields into an even smaller volume,[30] effectively forming a dielectric waveguide that can locally enhance the fields at the Au surface.[34] As a consequence, the maximum field enhancement at the Au surface β_{Au} increases from 35 to 200 (corresponding to an optical intensity enhancement from 1225 to 40 000) due to the combined effects of geometrical plasmon field enhancement and a secondary field enhancement from the plasmonic field confinement. It is worth highlighting that this secondary enhancement occurring at the metal surface is applicable to any plasmonic nanostructure supporting the antenna mode.[30]

In fact, metal−dielectric core−shell nanoparticles have been a staple in the plasmonics community[35] and have driven progress in diverse research lines including surface-enhanced Raman spectroscopy,[36] surface-enhanced fluorescence,[37] nanocomposite-assisted imaging,[38] catalysis,[39] and photovoltaics.[40] In recent years, the concept of enhancing fields *via* ultrathin high-refractive-index coatings that "trap" the enhanced fields has also been explored, *e.g.*, in core−shell nanoparticle dimers,[41] where a different plasmon mode—the bonding dipole plasmon (BDP) mode—was excited. Different from the antenna mode, the BDP mode has the maximally enhanced field located in the dimer gap (see Supporting Information S3). Nevertheless, the underlying enhancing mechanisms are similar:[41] (i) plasmonic field confinement following the boundary conditions at the dielectric−vacuum interface; (ii) high-refractive-index dielectric coating contributing to a strong light coupling effect in terms of improving the light absorption efficiency (see Figure 1a and Supporting Information S3).

In the current context, the tremendously increased field enhancement β_{Au} at the Au surface from the antenna mode is

https://dx.doi.org/10.1021/acsnano.0c03406
ACS Nano 2020, 14, 8806−8815

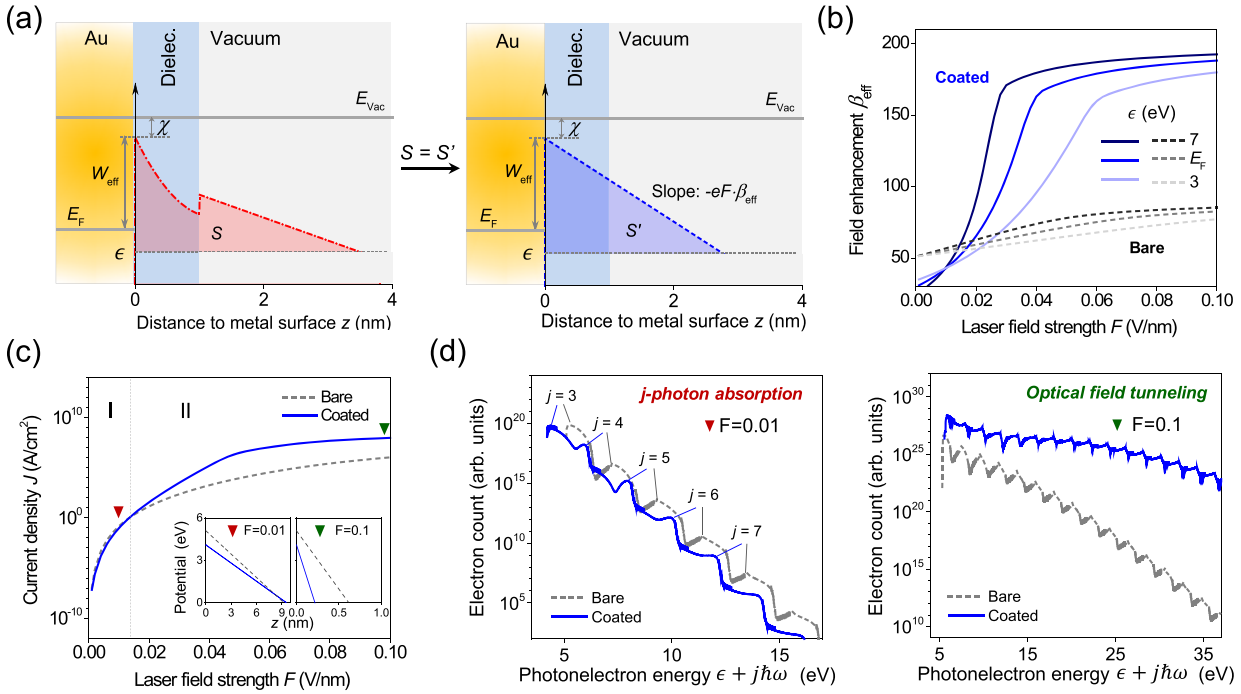

Figure 2. Theoretical modeling of double-barrier tunneling. (a) Triangular-barrier approximation: with a fixed effective work function $W_{eff} = W - \chi$, an effective field enhancement β_{eff} is defined for each electron initial energy ϵ to maintain the same area under the barriers: $S' = S$. (b) Calculated β_{eff} for three representative ϵ and (c) the photoemission current density J (the integration over all possible ϵ) as a function of the field strength of the incident laser F, for the bare or coated photoemitters. Inset: Triangular potential barriers for Fermi electrons ($\epsilon = E_F$) at two representative fields. (d) Photoelectron energy spectra *via* j-photon absorption (with respect to E_F) at $F = 0.01$ or 0.1 V/nm. In all calculations, the dielectric coating has $d = 1$ nm, $n = 1.5$, and $\chi = 0.9$ eV.

particularly desirable, which can vastly facilitate the photoemission process to operate at the optical field tunneling regime at a much lower incident field strength as explained below. To understand the photoemission process, we start with the time-dependent potential barrier $\phi(z, t)$ that is faced by the free electrons in Au to tunnel through and emit.[42−45] In the dielectric region, $0 < z < d$, it is written as:

$$\phi(z, t) = V_0 - eF\cos(\omega t)\int_0^z \beta(s)\,\mathrm{d}s \cong V_0 - eF\cos(\omega t)\left(\frac{\beta_D - \beta_{Au}}{2d}z^2 + \beta_{Au}z\right) \quad (1)$$

Here, z denotes the distance to the top surface of the Au tip; $V_0 = W + E_F - \chi$ is the nominal potential barrier height at the Au surface, where $W = 5.1$ eV and $E_F = 5.53$ eV are the work function and Fermi energy of Au and χ is the electron affinity of the dielectric layer; e is the elementary charge; $\omega = 2\pi c/\lambda$ denotes the angular frequency with the laser wavelength λ, where c is the speed of light in vacuum; and F represents the field strength of the incident laser. The optical near fields are taken care of by the exact enhancement profile that is extracted from our optical simulations and fitted using a linear function of distance, $\beta(z) = \beta_{Au} - (\beta_{Au} - \beta_D)z/d$, with $\beta(0) = \beta_{Au}$ at the Au surface and $\beta(d) = \beta_D$ at the dielectric/vacuum interface, respectively. In the free space region, $z > d$, the potential profile reads:

$$\phi(z, t) = W + E_F - eF\cos(\omega t)\left(\frac{\beta_{Au} - \beta_D}{2}d + \beta_D z\right) \quad (2)$$

where the field enhancement is assumed constant, β_D. To ensure a fair comparison, our optical simulations employ exactly the same settings for both bare and coated field emitters, but we set $n = 1$ to the dielectric for the bare emitter. As a result, the potential profiles described above also apply to the bare emitter, where we set the electron affinity $\chi = 0$ for the dielectric.

We plot in Figure 1c their potential barrier profiles $\phi(z, t = 0)$ induced by a different incident laser. Clearly, the presence of a dielectric coating not only reduces the height of the potential barrier due to the electron affinity of the dielectric layer χ but also significantly narrows the barrier, because of the much stronger field enhancement at the Au surface, β_{Au}. This barrier narrowing effect becomes even more profound for larger incident laser fields, as indicated by blue dashed lines in Figure 1c.

Double-Barrier Tunneling. Despite the barrier narrowing effect from the dielectric coatings, electrons inside the metal now need to overcome two barriers to get photoemitted (Figure 1c), for example *via* multiphoton absorption, photoassisted tunneling through either vacuum or the dielectric layer, or direct optical field tunneling. The probability for each of these processes depends on the electron initial energy ϵ and the overall potential barrier for a given incident laser field F. Here, ϵ is the longitudinal energy of electrons inside the metal impinging on the metal surface. To calculate the photoemission current, we employ a quantum theory of photoemission (see Methods),[6,20,21,46] which is the exact solution of the time-dependent Schrödinger equation subject to an oscillating triangular barrier. Therefore, we first need to approximate the irregular "double-barrier" potential profiles with an effective triangular barrier, as exemplified in Figure 2a. Here, the effective work function of the coated Au is fixed at $W_{eff} = W - \chi$. For an electron inside the

https://dx.doi.org/10.1021/acsnano.0c03406
ACS Nano 2020, 14, 8806−8815

metal with an initial energy ϵ, it would originally see an irregular potential barrier at the metal surface (left of Figure 2a). Correspondingly, the effective triangular barrier (right of Figure 2a) has the same barrier height as the original barrier, $W_{eff} + E_F - \epsilon$, for electrons at energy level ϵ, but with potential energy dropping linearly as a function of the distance away from the metal surface z. The area under the two barriers are kept the same (*cf.* the red-shaded area S *vs* the blue-shaded area S' in Figure 2a), from which the effective field enhancement factor $\beta_{eff}(\epsilon)$ can be determined for electrons with initial energy ϵ. As the area under the irregular double barrier changes nonlinearly with both the electron initial energy ϵ and the field strength of the incident laser F, the effective field enhancement factor β_{eff} is also a function of ϵ and F. This effective triangular-barrier approximation is plausible as the electron transmission is insensitive to the actual shape of the barrier, but is predominantly determined by the "area under the curve" according to the WKBJ approximation,[45,47] which has been previously verified for photoemission.[14−16,20] We also compare our quantum photoemission model based on this triangular-potential approximation to a double-barrier Fowler−Nordheim rate equation used in the "simple-man" model[48,49] (see Supporting Information S4). The two models show good agreement in the optical field tunneling regime, which unambiguously validates the effective triangular-barrier approximation in our quantum photoemission model.

In Figure 2b, we plot the ϵ-dependent effective optical field enhancement factor β_{eff} as a function of the field strength of the incident laser F at three representative electron initial energies ϵ for both coated and bare photoemitters. The coated emitter has improved β_{eff} over the bare emitter only for F exceeding a certain threshold, *e.g.*, 0.018 V/nm for Fermi electrons with $\epsilon = E_F$. This can be explained by the barrier profiles in Figure 1c. When F is small (black solid lines), the second barrier peak at the dielectric/vacuum interface can be higher than that at the Au surface. This results in β_{eff} smaller than that in the bare emitter due to the double-barrier profile. But when F is medium to large (blue dashed lines), the second barrier peak is lowered, and β_{eff} is predominantly determined by the significantly increased field enhancement at the Au surface β_{Au}.

The photoemission current density is then calculated:

$$J = e \int_0^\infty N(\epsilon)\, D(\epsilon)\, d\epsilon \tag{3}$$

where $N(\epsilon) = \frac{mk_BT}{2\pi^2\hbar^3} \ln\left[1 + \exp\left(\frac{E_F - \epsilon}{k_BT}\right)\right]$ represents the number density of electrons inside the metal impinging on the surface with longitudinal energy ϵ across unit area per unit time,[45] m is the electron mass, k_B is the Boltzmann constant, T is the temperature, and $\hbar$ is the reduced Planck constant. The electron emission probability $D(\epsilon)$ is calculated based on the quantum theory of photoemission (see Methods), which is the exact solution of the time-dependent Schrödinger equation subject to the triangular barrier shown in Figure 2a. As the linear size of the nanoemitter is about 40 nm in height, much longer than the electron de Broglie wavelength (~0.52 nm for Fermi electrons with $\epsilon = E_F = 5.53$ eV), the quantum model is appropriate to study the photoelectron emission. It is also worth highlighting that the model takes into account the contributions from all the possible j-photon absorption ($\epsilon + j\hbar\omega$) processes and is valid from multiphoton absorption to the optical field tunneling regime. Nevertheless, it should be noted that our model currently ignores the possible effects of charge trapping inside the coating dielectric[50,51] and space charge[52,53] in the potential barrier and electron transmission.

The calculated emission current density J as a function of the field strength of the incident laser F is shown in Figure 2c. In regime I where $F < 0.014$ V/nm, the emission current density from the coated Au tip is close to that from the bare tip, because of the smaller effective enhancement factor β_{eff}, as indicated by the lowered but widened barrier for Fermi electrons at $F = 0.01$ V/nm (inset). However, in regime II where $F > 0.014$ V/nm, the coated Au photoemitter outperforms the bare photoemitter, due to the combined effects of increased β_{eff} and lowered potential barrier, *e.g.*, for Fermi electrons at $F = 0.1$ V/nm (inset). For laser fields over a wide range of $F = 0.014-1$ V/nm, J from the coated photoemitter is enhanced by at least 2 orders of magnitude as compared to the bare emitter. The threshold laser field of 0.014 V/nm, at which the coated emitter outperforms the bare emitter, can also be derived when β_{eff} of the coated emitter exceeds that of the bare emitter for Fermi electrons, *i.e.*, 0.018 V/nm in Figure 2b. Interestingly, the increment of the current density J from the coated emitter slows down at higher incident laser fields $F > 0.05$ V/nm (Figure 2c), due to the saturation of β_{eff} at larger F (Figure 2b). The decreased slope suggests that the coated emitter has probably entered into the optical field tunneling regime, as it follows the Fowler−Nordheim current density scaling law[8,14] (see Supporting Information S4 for a comparison to the double-barrier Fowler−Nordheim rate equation[48,49]).

To better understand the photoemission mechanism, we plot the photoelectron energy spectra for two representative incident laser fields in Figure 2d. At $F = 0.01$ V/nm, the spectra exhibit distinct multiphoton peaks, whose magnitudes decay rapidly with energy. The dominant peaks correspond to three-photon absorption, as the ratio of barrier height to photon energy $W_{eff}/\hbar\omega > 2$ for both bare and coated photoemitters. At larger field $F = 0.1$ V/nm, the spectrum of the coated emitter becomes significantly broadened, reaching a plateau; meanwhile, the multiphoton peaks are severely smeared out. The broadening of the spectrum is ascribable to the increased contributions of higher-order photon processes at large incident laser fields,[20] as electrons need to absorb sufficient photon energy to overcome the increased ponderomotive energy, $U_p = e^2(\beta_{eff}F)^2/4m\omega^2$, in order to emit.[14,20,54] Classically, the plateau also signifies the back-propagation and rescatterings of electrons in an optical field tunneling process.[2,15,49] Therefore, the features of broadening and the plateau in the energy spectrum for the coated photoemitter indicate a more rapid transition from multiphoton absorption to optical field tunneling.[9,15,20] To be quantitative, the transition point can be indicatively determined by a local Keldysh parameter at the tip $\gamma_{loc} = \omega\sqrt{2mW_{eff}}/e\beta_{eff}F \approx 1$,[9,14,15,18,20] which gives a corresponding transition incident field strength of 0.10 (or 0.32) V/nm for the coated (or bare) field emitter. Alternatively, the transition point could be nominally marked by observing the termination of the scaling $J \propto F^{2j}$ with $j = 3$, which indicates the exit of the three-photon absorption regime, yielding a transition incident field strength of 0.05 (or 0.17) V/nm for the coated (or bare) field emitter. In either way, the coated emitter reaches the optical field tunneling regime at less than one-third of the incident laser field F as compared to the bare emitter. In other words, the optical field tunneling regime can be accessed at an incident laser intensity of about 10 times smaller with the dielectric coating.

https://dx.doi.org/10.1021/acsnano.0c03406
ACS Nano 2020, 14, 8806−8815

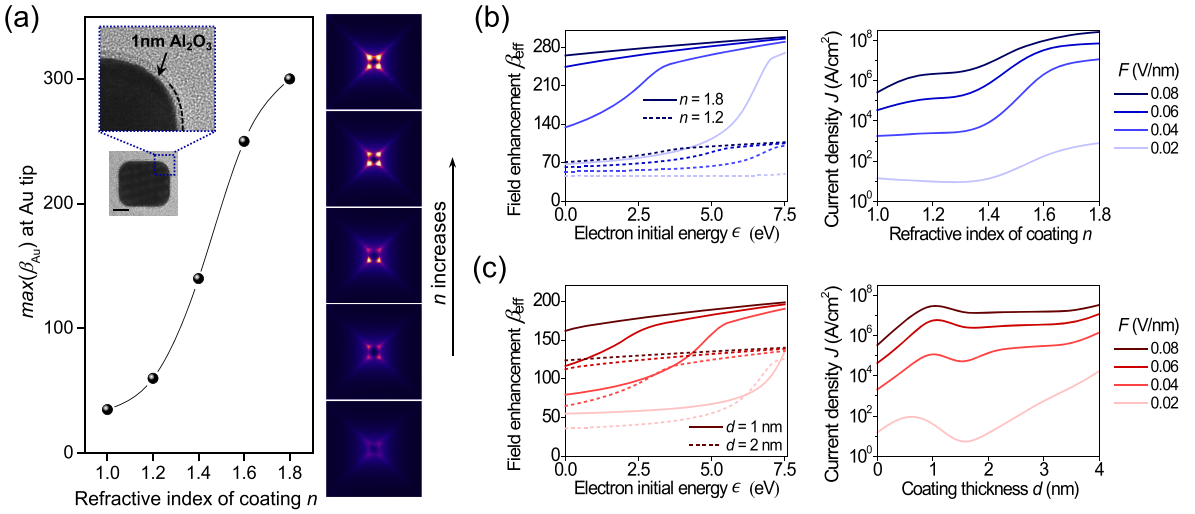

Figure 3. Effects of the dielectric coatings. (a) Dependence of the maximum field enhancement at Au tip max(β_{Au}) on the refractive index n of the dielectric coatings with fixed thickness d = 1 nm and the field enhancement profiles β_{Au} at the Au surface (top view). Inset: High-resolution transmission electron microscopy image of a Au nanoparticle coated with 1 nm thick Al_2O_3 (n = 1.7) *via* atomic layer deposition. (b) Effect of the index n on the effective field enhancement $\beta_{eff}(\epsilon)$ (left) and the resulting photoemission current density J (right), with fixed d = 1 nm and varied field strengths of the incident laser F. (c) Effect of the coating thickness d on $\beta_{eff}(\epsilon)$ (left) and J (right), with fixed n = 1.5 and varied F. In all calculations, χ = 0.9 eV, except χ = 0 and n = 1 for the bare photoemitter.

Dielectric Coatings. The example shown above has a fixed dielectric coating. In this section, we elaborate how the photoemission depends on the refractive index n and thickness d of the dielectric coatings, while the electron affinity χ = 0.9 eV is assumed constant, but set to zero for the bare emitter of n = 1. First, as n increases from 1 to 1.8, the plasmon resonant fields at the Au tip gradually squeeze into four bright points with the maximum field enhancement max(β_{Au}) reaching 300, as indicated in Figure 3a. This can be explained by the effect of the plasmon field confinement within the dielectric coating, particularly by the total internal reflection from the surrounding dielectric−vacuum interface back onto the Au surface, as illustrated in Figure 1b. The phenomenon occurs if the angle of incidence is greater than the critical angle $\theta_c = \sin^{-1}(1/n)$; for example, θ_c = 50° if n = 1.3; θ_c = 33° if n = 1.8. In other words, with increased n, more total internal reflections occur within the dielectric coating (as long as $\theta > \theta_c$), and therefore the plasmonic fields are better confined close to the Au surface. More information on this plasmonic field confinement effect (cross-sectional views) can be found in Supporting Information S3.

Taking this field enhancement into the potential barrier, we obtain the effective field enhancement factor β_{eff} near the corners of the emitter tip and the corresponding emission current density J, as shown in Figure 3b. In general, both β_{eff} and J increase as n increases, for a given incident laser field F. When the refractive index is small (n < 1.3), β_{eff} is relatively small and changes only slightly with the initial energies ϵ; thus the emission current density J is insensitive to the refractive index. However, when n becomes larger (n > 1.3), β_{eff} increases strongly as the initial electron energy ϵ gets closer to the Fermi level (E_F = 5.53 eV), resulting in a significant increase in the emission current density.

Similarly, we also studied the effect of coating thickness d from 0.5 to 4 nm as shown in Figure 3c, with a reference point set at d = 0 representing the bare photoemitter. Our optical simulations suggest that the field enhancement β_{Au} increases as d increases, reaches a maximum around d = 1 nm, and remains roughly a constant for d = 1.5−4 nm. The same trend is reflected in the emission current density J as a function of d. This is consistent with the behavior of β_{eff}, which shows a reduced dependence on ϵ when d > 1 nm. Here, the coating thickness of 0.5−4 nm is comparable to the spill-out distance of the electron wave function characterized by the Feibelman parameter in quantum plasmonics, which is in the angstrom range.[55−57] The shift of the induced surface charges with respect to the geometrical boundaries of the metal leads to an "effective" metal−dielectric interface inside the dielectric layer, making the dielectric coating effectively thinner in the classical sense.

It should be noted that the values of n and d studied here are within experimental reach; in the inset of Figure 3a, we show an image of a 1-nm-thick Al_2O_3 conformal coating around a gold nanoparticle that we obtained using atomic layer deposition. Besides, the constant χ = 0.9 eV is also a conservative assumption; in general, a larger χ is preferred.

Tunable Photoemission. We also investigate the geometric settings of the Au nanopyramid photoemitter, including a, κ, and h, to find out the possible tunability of the photoemission process. It is found that h is the most influential parameter to tune the resonance of the antenna mode (see Supporting Information S2), probably due to the perpendicular incident field along the height direction. In Figure 4a, when h is varied from a to 2a (a = 40 nm), the original single optical resonance at 608 nm gradually evolves into two peaks: mode A at 620 nm and mode B at 820 nm, respectively. Their optical near-field enhancement profile $\beta(y, z)$ is plotted in Figure 4b.

When this profile is taken into our photoemission model in eqs 1−3, we observe different emission current density profiles along the top surface of the Au tip as shown in Figure 4c, under the excitation of different lasers: 620 and 820 nm. In other words, the coated Au emitters can be customized to suit different laser sources to modulate the photoemission pattern and control the emission intensity. In this example, the magnitude of the emission current density is generally higher under the excitation of the 820 nm laser (lower photon energy) for a given field strength of the incident laser, due to the stronger field enhancements near the emitter tip as illustrated in Figure 4b.

https://dx.doi.org/10.1021/acsnano.0c03406
ACS Nano 2020, 14, 8806−8815

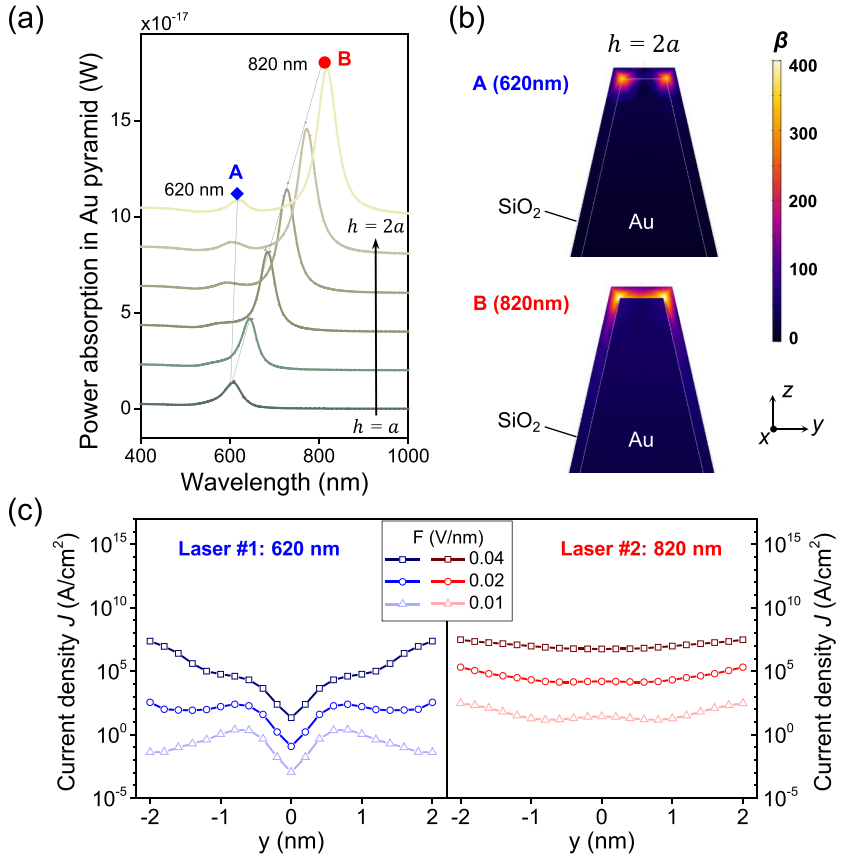

Figure 4. Tunable photoemission. (a) Tunable plasmon resonances by varying the height h of the Au-nanopyramid, with other parameters unchanged: a = 40 nm, κ = 0.1, d = 1 nm, n = 1.5, and χ = 0.9 eV. For a particular coated emitter with h = 80 nm: (b) optical field profiles for modes A and B near the apex of the emitter (cross-sectional view in the yz-plane); (c) photoemission current density J along the y-axis at the Au top surface under the illumination of lasers at two different wavelengths: 620 and 820 nm, corresponding to modes A and B, respectively.

It should be noted that the dominant photoemission process is three-photon absorption for both 620 and 820 nm laser excitations, as the ratio of barrier height to photon energy $W_{\text{eff}}/\hbar\omega > 2$ for both cases. Hence, the emission current is primarily determined by the local field strength and to a lesser degree by the photon energy, yielding a larger emission current from the 820 nm laser. The corresponding Keldysh parameter $\gamma_{\text{loc}} \approx 1$ suggests a transition from multiphoton absorption to optical field tunneling at an incident field strength as low as 0.03 V/nm.

CONCLUSIONS AND OUTLOOK

In summary, we have proposed to coat metal nanoemitters with an atomically thick dielectric to enhance photoemission, due to the combined effects of the significantly localized (hence enhanced) plasmon resonant fields and the reduced potential barrier induced by the coating. Our results indicate that dielectric coatings with higher refractive index can better confine and enhance the optical fields near the photoemitter tip, leading to a larger photoemission current. While the effect of coating thickness is less prominent, with an optimal thickness around 1 nm, we enjoy the freedom to choose a suitable thickness, *e.g.*, 1−4 nm, by placing greater emphasis on practical issues such as dielectric breakdown. We may consider ultrathin gate-oxide materials[58−62] such as SiO_2 and HfO_2 as our candidates. Furthermore, leveraging on multiple modes supported by a single coated emitter, we demonstrate a tunable resonant photoemission by using different ultrafast lasers.

Moving forward, our method is appropriate for studying nanoemitters of any shape and made of any material. We could extend our study to an array of coated emitters or combine dc bias and laser excitation to further improve the emission current at a given laser intensity. To do so, it is instructive to extend the current one-dimensional (1D) model to three-dimensional (3D)[14,54] under certain circumstances. It might be necessary to accurately model some high-dimensional effects, *e.g.*, 3D electron velocity distribution within an emitter, the corresponding angular distribution of the emitted electrons, and the nonuniformly distributed plasmonic near-fields around the nanoemitter tip. Including these effects, different emission mechanisms (multiphoton absorption or optical field tunneling) may coexist along the surface of the emitter at a given incident laser field strength, which could result in a different total emission current or a different energy distribution of the emitted electrons, deviating from the 1D prediction.

The suggested secondary enhancing mechanism *via* plasmonic field confinement can be directly applied to plasmon-induced hot carrier generation and applications involving metal nanoparticles.[63,64] The spill-out effect of the electron wave function in quantum plasmonics[55−57] could be analyzed for our plasmonic field confinement mechanism and also in the ultrafast regime.[65−67] On the other hand, our photoemission model can be further developed beyond a triangular-barrier approximation to characterize the photoemission through an irregular double-barrier potential profile. Meanwhile, our analytical photoemission model has shown excellent agreement with both

https://dx.doi.org/10.1021/acsnano.0c03406
ACS Nano 2020, 14, 8806−8815

experiments[6,16] and numerical solutions[20] for pulse durations down to 30 fs; it is instructive to include the effects of nonequilibrium heating[17,19] for even shorter pulse durations. This concept is also readily expandable beyond the metal nanoemitters and inorganic dielectrics studied here, such as alkane ligand,[68] graphene, and other 2D materials,[69,70] to advance the basic understanding of photoemission physics for novel materials and structures.[71]

METHODS

Full-Wave Optical Simulations. In our full-wave optical modeling, we consider a single Au nanopyramid sitting on a thin Au substrate and solve the scattering problem for such subwavelength conductive nanostructures in an oscillating electromagnetic field.[32,33] This is done by solving the full set of three-dimensional Maxwell's equations for the electric and magnetic fields using the finite element method. The permittivity of Au is taken from the Johnson and Christy handbook.[72] In our simulations, we assume that (i) the nanopyramid has side length $a = 40$ nm, height $h = 40$ nm, and aspect ratio $\kappa = 0.1$; (ii) the thin Au substrate has a side length of $a \times 5 = 200$ nm and thickness of 40 nm; (iii) the nanopyramid is coated with a dielectric layer with thickness d and refractive index n (the same settings are employed for both bare and coated emitters by setting $n = 1$ to the dielectric layer for the bare emitter) and embedded in vacuum; and (iv) plane-wave excitation from the side with a background electric field $|E_{0z}| = 1$ V/m perpendicular to the substrate plane.

Upon solving the electric and magnetic fields, the model calculates the spectrum of power absorption (*i.e.*, the volume integration of the resistive heating) inside the Au nanopyramid to identify the plasmonic resonant wavelengths (Figure 1a and Figure 4a). We then plot the spatial distributions of the calculated electric fields (normalized to the incident electric field $|E_{0z}| = 1$ V/m) at the resonant wavelength to illustrate the mode profile or the field enhancement profile $\beta(x, y, z)$ (Figure 1b and Figure 4b). The exact field enhancement profile $\beta(x, y, z)$ can also be exported from the optical simulations to calculate the potential barrier defined in eq 1. All these calculations are performed based on the scattered-field formulation in the COMSOL Multiphysics, RF module, and a perfectly matched layer (PML) boundary is applied to eliminate the back reflections of the incident radiation.

Quantum Theory of Photoemission. A quantum mechanical model[6,20,21,46] is used to calculate the photoelectron emission current density from both bare and coated metal surfaces driven by laser fields. The model is assumed to be one-dimensional, in which electrons impinge normally to the metal surface. It assumes that the incident laser field is perpendicular to the metal surface and cuts off abruptly at the metal surface, which is justified by the much smaller laser penetration depth compared with the laser wavelength.

With the assumptions listed above, the electron wave function $\psi(z, t)$ is solved exactly from the time-dependent Schrödinger equation:

$$i\hbar\frac{\partial\psi(z,t)}{\partial t} = -\frac{\hbar^2}{2m}\frac{\partial^2\psi(z,t)}{\partial z^2} + \phi(z,t)\psi(z,t) \tag{4}$$

where $\hbar$ is the reduced Planck constant, m is the electron mass, z is the distance to the metal surface, and $\phi(z, t)$ is the potential barrier:

$$\phi(z,t) = \begin{cases} 0, & z < 0 \\ W_{\text{eff}} + E_{\text{F}} - eF_{\text{eff}}z\cos(\omega t), & z \geq 0 \end{cases} \tag{5}$$

where W_{eff} and E_{F} are the effective work function and Fermi energy of the metal, respectively; $F_{\text{eff}} = \beta_{\text{eff}}F$ is the effective near-field experienced by the tunneling electrons, and ω denotes the angular frequency of the incident laser field F. In the calculation, W_{eff} and F_{eff} are taken from the triangular-barrier approximation in Figure 2a.

Based on this oscillating triangular barrier, exact analytical solutions are obtained[6,20,21,46] for the incident electron wave ψ_{i} inside the metal and transmitted electron wave ψ_{t} outside the metal using Truscott transformations[73] from eq 4, which read:

$$\begin{aligned}\psi_i(z,t) &= \exp\left[-i\left(\frac{\epsilon}{\hbar}\right)t + ik_0 z\right] \\ &+ \sum_{j=-\infty}^{\infty} R_j \exp\left[-i\left(\frac{\epsilon + j\hbar\omega}{\hbar}\right)t - ik_j z\right], \\ \psi_t(z,t) &= \sum_{j=-\infty}^{\infty} T_j \exp\left[i\sqrt{\frac{2mE_j}{\hbar^2}}\xi\right]\exp\left[-i\left(\frac{\epsilon + j\hbar\omega}{\hbar}\right)t\right] \\ &\times \exp\left[i\left(\frac{eF_{\text{eff}}\sin(\omega t)}{\hbar\omega}\right)z + i\frac{e^2F_{\text{eff}}^2\sin(2\omega t)}{8\hbar m\omega^3}\right]\end{aligned} \tag{6}$$

where ϵ is the electron initial energy, $k_0 = \sqrt{2m\epsilon/\hbar^2}$ and $k_j = \sqrt{2m(\epsilon + j\hbar\omega)/\hbar^2}$ are the electron wave numbers, T_j (or R_j) is the electron wave transmission (or reflection) coefficient, $E_j = \epsilon + j\hbar\omega - W_{\text{eff}} - E_{\text{F}} - U_{\text{P}}$ with ponderomotive energy $U_{\text{P}} = e^2F_{\text{eff}}^2/4m\omega^2$, the parameter $\xi = z + eF_{\text{eff}}\cos(\omega t)/m\omega^2$, and the integer j indicates the j-photon process.

Applying boundary conditions that both $\psi(z, t)$ and $\partial\psi(z, t)/\partial z$ are continuous at the metal–vacuum interface (for bare metal) or metal–dielectric interface (for coated metal), we obtain the following relationship:

$$2\sqrt{\epsilon}\,\delta(l) = \sum_{j=-\infty}^{\infty} T_j\left[\sqrt{\epsilon + l\hbar\omega}\,P_{j(j-l)} + \frac{\hbar}{\sqrt{2m}}Q_{j(j-l)}\right] \tag{7}$$

Here, δ is the Dirac delta function, $P_{j(j-l)} = (1/2\pi)\int_0^{2\pi} p_j(\omega t)\exp[-i(j-l)\omega t]\,\mathrm{d}(\omega t)$ and $Q_{j(j-l)} = (1/2\pi)\int_0^{2\pi} q_j(\omega t)\exp[-i(j-l)\omega t]\,\mathrm{d}(\omega t)$ are the $(j-l)$th Fourier transform coefficients of $p_j(\omega t)$ and $q_j(\omega t)$:

$$\begin{aligned} p_j(\omega t) &= \exp\left[i\sqrt{2mE_j}\frac{eF_{\text{eff}}\cos(\omega t)}{m\hbar\omega^2} + i\frac{e^2F_{\text{eff}}^2\sin(2\omega t)}{8m\hbar\omega^3}\right], \\ q_j(\omega t) &= \left[\frac{\sqrt{2mE_j}}{\hbar} + \frac{eF_{\text{eff}}\sin(\omega t)}{\hbar\omega}\right]\exp\left[i\sqrt{2mE_j}\frac{eF_{\text{eff}}\cos(\omega t)}{m\hbar\omega^2}\right. \\ &\left. + i\frac{e^2F_{\text{eff}}^2\sin(2\omega t)}{8m\hbar\omega^3}\right] \end{aligned} \tag{8}$$

With the electron transmission coefficient T_j solved from eq 7, the time-averaged electron transmission probability *via* the j-photon process for an initial energy of ϵ is given as:

$$\langle w_j(\epsilon)\rangle = \mathrm{Im}\left(i\frac{\sqrt{E_j}}{\sqrt{\epsilon}}|T_j|^2\right) \tag{9}$$

and the total electron transmission probability for an initial energy of ϵ is a sum of $\langle w_j\rangle$ through all the j-photon processes:

$$D(\epsilon) = \sum_{j=-\infty}^{\infty}\langle w_j(\epsilon)\rangle \tag{10}$$

With this transmission probability $D(\epsilon)$, the photoemission current density J can be calculated from eq 3 in the main text.

ASSOCIATED CONTENT

Supporting Information

The Supporting Information is available free of charge at https://pubs.acs.org/doi/10.1021/acsnano.0c03406.

Excitation of the antenna mode; geometry of the nanopyramid; effects of coating on the antenna mode; validation of the triangular-barrier approximation; Figures S1–S4 (PDF)

https://dx.doi.org/10.1021/acsnano.0c03406
ACS Nano 2020, 14, 8806–8815

AUTHOR INFORMATION

Corresponding Authors

Peng Zhang − *Department of Electrical and Computer Engineering, Michigan State University, East Lansing, Michigan 48824-1226, United States;* orcid.org/0000-0003-0606-6855; Email: pz@egr.msu.edu

Lin Wu − *Institute of High Performance Computing, Agency for Science, Technology, and Research (A*STAR), Singapore 138632;* orcid.org/0000-0002-3188-0640; Email: wul@ihpc.a-star.edu.sg

Authors

Xiao Xiong − *Institute of High Performance Computing, Agency for Science, Technology, and Research (A*STAR), Singapore 138632;* orcid.org/0000-0002-7153-8081

Yang Zhou − *Department of Electrical and Computer Engineering, Michigan State University, East Lansing, Michigan 48824-1226, United States*

Yi Luo − *Department of Electrical and Computer Engineering, Michigan State University, East Lansing, Michigan 48824-1226, United States*

Xiang Li − *Leadmicro Nano Technology Co., Ltd, Wuxi 214000, China*

Michel Bosman − *Department of Materials Science and Engineering, National University of Singapore, Singapore 117575; Institute of Materials Research and Engineering, Agency for Science, Technology, and Research (A*STAR), Singapore 138634;* orcid.org/0000-0002-8717-7655

Lay Kee Ang − *SUTD-MIT International Design Center, Science, Mathematics and Technology Cluster, Singapore University of Technology and Design (SUTD), Singapore 487372;* orcid.org/0000-0003-2811-1194

Complete contact information is available at: https://pubs.acs.org/10.1021/acsnano.0c03406

Author Contributions

#X. Xiong and Y. Zhou contributed equally.

Notes

The authors declare no competing financial interest.

ACKNOWLEDGMENTS

The Institute of High Performance Computing (IHPC) acknowledges financial support from the National Research Foundation Singapore NRF2017-NRF-NSFC002-015 and A*STAR SERC A1685b0005. Y.Z., Y.L., and P.Z. were supported by the Air Force Office of Scientific Research (AFOSR) YIP Grant No. FA9550-18-1-0061 and the Office of Naval Research (ONR) YIP Grant No. N00014-20-1-2681. We thank C. A. Nijhuis and S. F. Tan (NUS) for the synthesis of the gold nanoparticles.

REFERENCES

(1) Tsujino, S.; Beaud, P.; Kirk, E.; Vogel, T.; Sehr, H.; Gobrecht, J.; Wrulich, A. Ultrafast Electron Emission from Metallic Nanotip Arrays Induced by Near Infrared Femtosecond Laser Pulses. *Appl. Phys. Lett.* **2008**, *92*, 193501.

(2) Krüger, M.; Schenk, M.; Hommelhoff, P. Attosecond Control of Electrons Emitted from a Nanoscale Metal Tip. *Nature* **2011**, *475*, 78.

(3) Park, D. J.; Piglosiewicz, B.; Schmidt, S.; Kollmann, H.; Mascheck, M.; Lienau, C. Strong Field Acceleration and Steering of Ultrafast Electron Pulses from a Sharp Metallic Nanotip. *Phys. Rev. Lett.* **2012**, *109*, 244803.

(4) Förster, M.; Paschen, T.; Krüger, M.; Lemell, C.; Wachter, G.; Libisch, F.; Madlener, T.; Burgdörfer, J.; Hommelhoff, P. Two-Color Coherent Control of Femtosecond Above-Threshold Photoemission from a Tungsten Nanotip. *Phys. Rev. Lett.* **2016**, *117*, 217601.

(5) Echternkamp, K.; Herink, G.; Yalunin, S. V.; Rademann, K.; Schäfer, S.; Ropers, C. Strong-Field Photoemission in Nanotip Near-Fields: from Quiver to Sub-Cycle Electron Dynamics. *Appl. Phys. B: Lasers Opt.* **2016**, *122*, 80.

(6) Luo, Y.; Zhang, P. Ultrafast Strong-Field Photoelectron Emission Due to Two-Color Laser Fields. *Phys. Rev. B: Condens. Matter Mater. Phys.* **2018**, *98*, 165442.

(7) Zewail, A. H. Four-Dimensional Electron Microscopy. *Science* **2010**, *328*, 187−193.

(8) Hommelhoff, P.; Sortais, Y.; Aghajani-Talesh, A.; Kasevich, M. A. Field Emission Tip as a Nanometer Source of Free Electron Femtosecond Pulses. *Phys. Rev. Lett.* **2006**, *96*, No. 077401.

(9) Piglosiewicz, B.; Schmidt, S.; Park, D. J.; Vogelsang, J.; Groß, P.; Manzoni, C.; Farinello, P.; Cerullo, G.; Lienau, C. Carrier-Envelope Phase Effects on the Strong-Field Photoemission of Electrons from Metallic Nanostructures. *Nat. Photonics* **2014**, *8*, 37.

(10) Forati, E.; Dill, T. J.; Tao, A. R.; Sievenpiper, D. Photoemission-Based Microelectronic Devices. *Nat. Commun.* **2016**, *7*, 13399.

(11) Zhang, P.; Lau, Y. Ultrafast and Nanoscale Diodes. *J. Plasma Phys.* **2016**, *82*, 595820505.

(12) Zhang, P.; Valfells, Á.; Ang, L.; Luginsland, J.; Lau, Y. 100 Years of the Physics of Diodes. *Appl. Phys. Rev.* **2017**, *4*, No. 011304.

(13) Yanagisawa, H.; Hengsberger, M.; Leuenberger, D.; Klöckner, M.; Hafner, C.; Greber, T.; Osterwalder, J. Energy Distribution Curves of Ultrafast Laser-Induced Field Emission and Their Implications for Electron Dynamics. *Phys. Rev. Lett.* **2011**, *107*, No. 087601.

(14) Yalunin, S. V.; Gulde, M.; Ropers, C. Strong-Field Photoemission from Surfaces: Theoretical Approaches. *Phys. Rev. B: Condens. Matter Mater. Phys.* **2011**, *84*, 195426.

(15) Herink, G.; Solli, D. R.; Gulde, M.; Ropers, C. Field-Driven Photoemission from Nanostructures Quenches the Quiver Motion. *Nature* **2012**, *483*, 190−193.

(16) Ropers, C.; Solli, D.; Schulz, C.; Lienau, C.; Elsaesser, T. Localized Multiphoton Emission of Femtosecond Electron Pulses from Metal Nanotips. *Phys. Rev. Lett.* **2007**, *98*, No. 043907.

(17) Wu, L.; Ang, L. K. Nonequilibrium Model of Ultrafast Laser-Induced Electron Photofield Emission from a DC-Biased Metallic Surface. *Phys. Rev. B: Condens. Matter Mater. Phys.* **2008**, *78*, 224112.

(18) Pant, M.; Ang, L. K. Ultrafast Laser-Induced Electron Emission from Multiphoton to Optical Tunneling. *Phys. Rev. B: Condens. Matter Mater. Phys.* **2012**, *86*, No. 045423.

(19) Pant, M.; Ang, L. Time-Dependent Quantum Tunneling and Nonequilibrium Heating Model for the Generalized Einstein Photoelectric Effect. *Phys. Rev. B: Condens. Matter Mater. Phys.* **2013**, *88*, 195434.

(20) Zhang, P.; Lau, Y. Ultrafast Strong-Field Photoelectron Emission from Biased Metal Surfaces: Exact Solution to Time-Dependent Schrödinger Equation. *Sci. Rep.* **2016**, *6*, 19894.

(21) Luo, Y.; Zhang, P. Analysis of Two-Color Laser-Induced Electron Emission from a Biased Metal Surface Using an Exact Quantum Mechanical Solution. *Phys. Rev. Appl.* **2019**, *12*, No. 044056.

(22) Maier, S. A. *Plasmonics: Fundamentals and Applications*; Springer-Verlag New York Inc.: New York, NY, USA, 2007; pp 65−88.

(23) Dombi, P.; Horl, A.; Racz, P.; Marton, I.; Trugler, A.; Krenn, J. R.; Hohenester, U. Ultrafast Strong-Field Photoemission from Plasmonic Nanoparticles. *Nano Lett.* **2013**, *13*, 674−678.

(24) Kusa, F.; Echternkamp, K.; Herink, G.; Ropers, C.; Ashihara, S. Optical Field Emission from Resonant Gold Nanorods Driven by Femtosecond Mid-Infrared Pulses. *AIP Adv.* **2015**, *5*, No. 077138.

(25) Putnam, W. P.; Hobbs, R. G.; Keathley, P. D.; Berggren, K. K.; Kärtner, F. X. Optical-Field-Controlled Photoemission from Plasmonic Nanoparticles. *Nat. Phys.* **2017**, *13*, 335.

(26) Ludwig, M.; Aguirregabiria, G.; Ritzkowsky, F.; Rybka, T.; Marinica, D. C.; Aizpurua, J.; Borisov, A. G.; Leitenstorfer, A.; Brida, D.

Sub-Femtosecond Electron Transport in a Nanoscale Gap. *Nat. Phys.* **2020**, *16*, 341−345.
(27) Sivis, M.; Pazos-Perez, N.; Yu, R.; Alvarez-Puebla, R.; de Abajo, F. J. G.; Ropers, C. Continuous-Wave Multiphoton Photoemission from Plasmonic Nanostars. *Commun. Phys.* **2018**, *1*, 13.
(28) Wang, W.; Guo, B.; Dai, H.; Zhao, C.; Xie, G.; Ma, R.; Akram, M. Z.; Shan, H.; Cai, C.; Fang, Z.; Gong, J. R. Improving Water Oxidation Efficiency by Light-Induced Electric Field in Nanograting Photoanodes. *Nano Lett.* **2019**, *19*, 6133−6139.
(29) Tan, S. F.; Wu, L.; Yang, J. K. W.; Bai, P.; Bosman, M.; Nijhuis, C. A. Quantum Plasmon Resonances Controlled by Molecular Tunnel Junctions. *Science* **2014**, *343*, 1496−1499.
(30) Xiong, X.; You, J.-B.; Bai, P.; Png, C. E.; Zhou, Z.-K.; Wu, L. Ultrastrong Coupling in Single Plexcitonic Nanocubes. *Nanophotonics* **2020**, *9*, 257.
(31) Hentschel, M.; Wu, L.; Schaferling, M.; Bai, P.; Li, E. P.; Giessen, H. Optical Properties of Chiral Three-Dimensional Plasmonic Oligomers at the Onset of Charge-Transfer Plasmons. *ACS Nano* **2012**, *6*, 10355−10365.
(32) Wu, L.; Duan, H.; Bai, P.; Bosman, M.; Yang, J. K. W.; Li, E. Fowler−Nordheim Tunneling Induced Charge Transfer Plasmons between Nearly Touching Nanoparticles. *ACS Nano* **2013**, *7*, 707−716.
(33) Huang, Y.; Wu, L.; Chen, X.; Bai, P.; Kim, D.-H. Synthesis of Anisotropic Concave Gold Nanocuboids with Distinctive Plasmonic Properties. *Chem. Mater.* **2013**, *25*, 2470−2475.
(34) Davis, T. J.; Gómez, D. E.; Roberts, A. Plasmonic Circuits for Manipulating Optical Information. *Nanophotonics* **2016**, *6*, 543−559.
(35) Hanske, C.; Sanz-Ortiz, M. N.; Liz-Marzán, L. M. Silica-Coated Plasmonic Metal Nanoparticles in Action. *Adv. Mater.* **2018**, *30*, 1707003.
(36) Li, J. F.; Huang, Y. F.; Ding, Y.; Yang, Z. L.; Li, S. B.; Zhou, X. S.; Fan, F. R.; Zhang, W.; Zhou, Z. Y.; Ren, B.; Wang, Z. L.; Tian, Z. Q. Shell-Isolated Nanoparticle-Enhanced Raman Spectroscopy. *Nature* **2010**, *464*, 392−395.
(37) Bardhan, R.; Grady, N. K.; Halas, N. J. Nanoscale Control of Near-Infrared Fluorescence Enhancement Using Au Nanoshells. *Small* **2008**, *4*, 1716−1722.
(38) Hembury, M.; Chiappini, C.; Bertazzo, S.; Kalber, T. L.; Drisko, G. L.; Ogunlade, O.; Walker-Samuel, S.; Krishna, K. S.; Jumeaux, C.; Beard, P.; Kumar, C. S. S. R.; Porter, A. E.; Lythgoe, M. F.; Boissière, C.; Sanchez, C.; Stevens, M. M. Gold−Silica Quantum Rattles for Multimodal Imaging and Therapy. *Proc. Natl. Acad. Sci. U. S. A.* **2015**, *112*, 1959−1964.
(39) Zhang, T.; Zhao, H.; He, S.; Liu, K.; Liu, H.; Yin, Y.; Gao, C. Unconventional Route to Encapsulated Ultrasmall Gold Nanoparticles for High-Temperature Catalysis. *ACS Nano* **2014**, *8*, 7297−7304.
(40) Jankovic, V.; Yang, Y.; You, J.; Dou, L.; Liu, Y.; Cheung, P.; Chang, J. P.; Yang, Y. Active Layer-Incorporated, Spectrally Tuned Au/Sio2 Core/Shell Nanorod-Based Light Trapping for Organic Photovoltaics. *ACS Nano* **2013**, *7*, 3815−3822.
(41) Zhai, Y.; Deng, L.; Chen, Y.; Wang, N.; Huang, Y. Reducing the Loss of Electric Field Enhancement for Plasmonic Core−Shell Nanoparticle Dimers by High Refractive Index Dielectric Coating. *J. Phys.: Condens. Matter* **2020**, *32*, 105001.
(42) Keldysh, L. V. Ionization in the Field of a Strong Electromagnetic Wave. *J. Exp. Theor. Phys.* **1965**, *20*, 1307.
(43) Landau, L. D.; Lifshitz, E. M. *Quantum Mechanics: Non-Relativistic Theory*; Pergamon Press: Oxford, UK, 1965; pp 171−177.
(44) Büttiker, M.; Landauer, R. Traversal Time for Tunneling. *Phys. Rev. Lett.* **1982**, *49*, 1739−1742.
(45) Jensen, K. L. *Introduction to the Physics of Electron Emission*, 1st ed.; John Wiley and Sons Ltd: Hoboken, NJ, USA, 2017; pp 127−148.
(46) Zhou, Y.; Zhang, P. A Quantum Model for Photoemission from Metal Surfaces and Its Comparison With the Three-Step Model and Fowler−Dubridge Model. *J. Appl. Phys.* **2020**, *127*, 164903.
(47) Bohm, D. *Quantum Theory*; Dover Publications Inc.: New York, USA, 1951; pp 264−295.
(48) Huang, Q.-A. Instability of Field Emission from Silicon Covered with a Thin Oxide Due to Electron Trapping. *J. Appl. Phys.* **1996**, *79*, 3703−3707.
(49) Keathley, P. D.; Sell, A.; Putnam, W. P.; Guerrera, S.; Velásquez-García, L.; Kärtner, F. X. Strong-Field Photoemission from Silicon Field Emitter Arrays. *Ann. Phys. (Berlin, Ger.)* **2013**, *525*, 144−150.
(50) Rose, A. Space-Charge-Limited Currents in Solids. *Phys. Rev.* **1955**, *97*, 1538−1544.
(51) Frank, R. I.; Simmons, J. G. Space-Charge Effects on Emission-Limited Current Flow in Insulators. *J. Appl. Phys.* **1967**, *38*, 832−840.
(52) Zhang, P. Scaling for Quantum Tunneling Current in Nano- and Subnano-Scale Plasmonic Junctions. *Sci. Rep.* **2015**, *5*, 9826.
(53) Banerjee, S.; Zhang, P. A Generalized Self-Consistent Model for Quantum Tunneling Current in Dissimilar Metal-Insulator-Metal Junction. *AIP Adv.* **2019**, *9*, No. 085302.
(54) Bormann, R.; Gulde, M.; Weismann, A.; Yalunin, S.; Ropers, C. Tip-Enhanced Strong-Field Photoemission. *Phys. Rev. Lett.* **2010**, *105*, 147601.
(55) Toscano, G.; Straubel, J.; Kwiatkowski, A.; Rockstuhl, C.; Evers, F.; Xu, H.; Mortensen, N. A.; Wubs, M. Resonance Shifts and Spill-Out Effects in Self-Consistent Hydrodynamic Nanoplasmonics. *Nat. Commun.* **2015**, *6*, 1−11.
(56) Ciraci, C.; Della Sala, F. Quantum Hydrodynamic Theory for Plasmonics: Impact of The Electron Density Tail. *Phys. Rev. B: Condens. Matter Mater. Phys.* **2016**, *93*, 205405.
(57) Zhu, W.; Esteban, R.; Borisov, A. G.; Baumberg, J. J.; Nordlander, P.; Lezec, H. J.; Aizpurua, J.; Crozier, K. B. Quantum Mechanical Effects in Plasmonic Structures with Subnanometre Gaps. *Nat. Commun.* **2016**, *7*, DOI: 10.1038/ncomms11495.
(58) Lombardo, S.; Stathis, J. H.; Linder, B. P.; Pey, K. L.; Palumbo, F.; Tung, C. H. Dielectric Breakdown Mechanisms in Gate Oxides. *J. Appl. Phys.* **2005**, *98*, 12.
(59) Lo, V. L.; Pey, K. L.; Tung, C. H.; Li, X. Multiple Digital Breakdowns and Its Consequence on Ultrathin Gate Dielectrics Reliability Prediction. In *2007 IEEE International Electron Devices Meeting*; Washington, DC, USA, Dec 10−12, 2007; IEEE: Piscataway, NJ, 2008; pp 497−500; IEEE Xplore. https://ieeexplore.ieee.org/document/4418983 (accessed June 18, 2020).
(60) Li, X.; Tung, C.; Pey, K.; Lo, V. The Physical Origin of Random Telegraph Noise after Dielectric Breakdown. *Appl. Phys. Lett.* **2009**, *94*, 132904.
(61) Li, X.; Pey, K.; Bosman, M.; Liu, W.; Kauerauf, T. Direct Visualization and In-Depth Physical Study of Metal Filament Formation in Percolated High-κ Dielectrics. *Appl. Phys. Lett.* **2010**, *96*, No. 022903.
(62) Veloso, A.; Ragnarsson, L.-Å.; Cho, M.; Devriendt, K.; Kellens, K.; Sebaai, F.; Suhard, S.; Brus, S.; Crabbe, Y.; Schram, T.; Röhr, E.; Paraschiv, V.; Eneman, G.; Kauerauf, T.; Dehan, M.; Hong, S.-H.; Yamaguchi, S.; Takeoka, S.; Higuchi, Y.; Tielens, H.; et al. Gate-Last *vs.* Gate-First Technology for Aggressively Scaled EOT Logic/RF CMOS. In *2011 Symposium on VLSI Technology-Digest of Technical Papers*, Honolulu, HI, USA, Jun 14−16, 2011; IEEE: Piscataway, NJ, 2011; pp 34−35; IEEE Xplore. https://ieeexplore.ieee.org/document/5984619 (accessed June 18, 2020).
(63) Manjavacas, A.; Liu, J. G.; Kulkarni, V.; Nordlander, P. Plasmon-Induced Hot Carriers in Metallic Nanoparticles. *ACS Nano* **2014**, *8*, 7630−7638.
(64) Liu, J. G.; Zhang, H.; Link, S.; Nordlander, P. Relaxation of Plasmon-Induced Hot Carriers. *ACS Photonics* **2018**, *5*, 2584−2595.
(65) Voisin, C.; Christofilos, D.; Del Fatti, N.; Vallée, F.; Prével, B.; Cottancin, E.; Lermé, J.; Pellarin, M.; Broyer, M. Size-Dependent Electron-Electron Interactions in Metal Nanoparticles. *Phys. Rev. Lett.* **2000**, *85*, 2200.
(66) Li, X.; Fang, H.; Weng, X.; Zhang, L.; Dou, X.; Yang, A.; Yuan, X. Electronic Spill-Out Induced Spectral Broadening in Quantum Hydrodynamic Nanoplasmonics. *Opt. Express* **2015**, *23*, 29738−29745.
(67) Ding, W. J.; Lim, J. Z. J.; Do, H. T. B.; Xiong, X.; Mahfoud, Z.; Png, C. E.; Bosman, M.; Ang, L. K.; Wu, L. Particle Simulation of Plasmons. *Nanophotonics* **2020**, DOI: 10.1515/nanoph−2020−0067.

https://dx.doi.org/10.1021/acsnano.0c03406
ACS Nano 2020, 14, 8806−8815

(68) Xie, X. N.; Gao, X.; Qi, D.; Xie, Y.; Shen, L.; Yang, S.-W.; Sow, C. H.; Wee, A. T. S. Chemically Linked AuNP-Alkane Network for Enhanced Photoemission and Field Emission. *ACS Nano* **2009**, *3*, 2722−2730.
(69) Ang, Y. S.; Yang, H. Y.; Ang, L. Universal Scaling Laws in Schottky Heterostructures Based on Two-Dimensional Materials. *Phys. Rev. Lett.* **2018**, *121*, No. 056802.
(70) Heide, C.; Hauck, M.; Higuchi, T.; Ristein, J.; Ley, L.; Weber, H. B.; Hommelhoff, P. Attosecond-Fast Internal Photoemission. *Nat. Photonics* **2020**, *14*, 219−222.
(71) Dombi, P.; Pápa, Z.; Vogelsang, J.; Yalunin, S. V.; Sivis, M.; Herink, G.; Schäfer, S.; Groß, P.; Ropers, C.; Lienau, C. Strong-Field Nano-Optics. *Rev. Mod. Phys.* **2020**, *92*, No. 025003.
(72) Johnson, P. B.; Christy, R.-W. Optical Constants of the Noble Metals. *Phys. Rev. B* **1972**, *6*, 4370.
(73) Truscott, W. Wave Functions in the Presence of a Time-Dependent Field: Exact Solutions and Their Application to Tunneling. *Phys. Rev. Lett.* **1993**, *70*, 1900.

https://dx.doi.org/10.1021/acsnano.0c03406
ACS Nano 2020, 14, 8806−8815

Supporting Information: Plasmon-Enhanced Resonant Photoemission Using Atomically-Thick Dielectric Coatings

Xiao Xiong,[†,#] Yang Zhou,[‡,#] Yi Luo,[‡] Xiang Li,[¶] Michel Bosman,[§,‖] Lay Kee Ang,[⊥] Peng Zhang,[*,‡] and Lin Wu[*,†]

†*Institute of High Performance Computing, Agency for Science, Technology, and Research (A*STAR), 1 Fusionopolis Way, #16-16 Connexis, Singapore 138632.*

‡*Department of Electrical and Computer Engineering, Michigan State University, East Lansing, MI 48824-1226 USA.*

¶*Leadmicro Nano Technology Co., Ltd, 7 Xingchuang Road, Wuxi 214000, China.*

§*Department of Materials Science and Engineering, National University of Singapore, 9 Engineering Drive 1, Singapore 117575.*

‖*Institute of Materials Research and Engineering, Agency for Science, Technology, and Research (A*STAR), 2 Fusionopolis Way, Singapore 138634.*

⊥*SUTD-MIT International Design Center, Science, Mathematics and Technology Cluster, Singapore University of Technology and Design (SUTD), 8 Somapah Road, Singapore 487372.*

#*These two authors contributed equally.*

E-mail: pz@egr.msu.edu; wul@ihpc.a-star.edu.sg

S1. Excitation of Antenna Mode

The antenna mode in our nanopyramid-emitter configuration has very bright hotspots at the upper tip originating from the mirror effect, *i.e.*, the coupling between metal nanoemitter and metal substrate. The efficient excitation of the antenna mode depends on the substrate and the polarization of the incident light. As shown in Fig. S1, different scenarios are compared to the case in Fig. 1 in the main text (*i.e.*, Au substrate and vertical polarization). With glass substrate in Fig. S1(b) or horizontal polarization in Fig. S1(c), both the light absorption efficiency and the field enhancement drop. The results also suggest that the vertical polarization is more critical than the metal substrate.

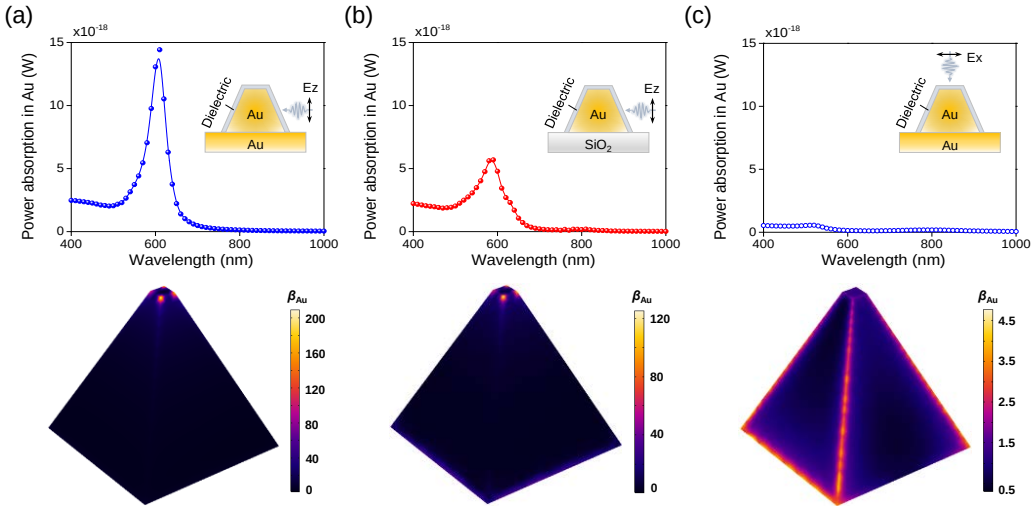

Figure S1: Excitation of antenna mode. The spectra of absorption in nanoemitter (top panel) and the field enhancement profiles around the Au surface (bottom panel) for different scenarios illustrated in the insets: (a) field emitter on Au substrate excited by vertical polarization (Fig. 1 in main text); (b) field emitter on glass substrate excited by vertical polarization; (c) field emitter on Au substrate excited by horizontal polarization. In all cases, the nanoemitter has the same geometry with side length $a = 40$ nm, height $h = 40$ nm, aspect ratio $\kappa = 0.1$, and dielectric coating of thickness $d = 1$ nm and refractive index $n = 1.5$.

S2. Geometry of Nanopyramid

All the geometrical parameters of nanopyramid can be used to design and tune the resonance of plasmon antenna mode. In Fig. S2, we show that the absorption peak in a nanopyramid shifts as its geometry changes, such as aspect ratio κ, side length a, and height h. As long as the antenna mode is efficiently excited by the vertical polarization, we have a good nanoemitter. The absorption peak only matters the choice of excitation laser.

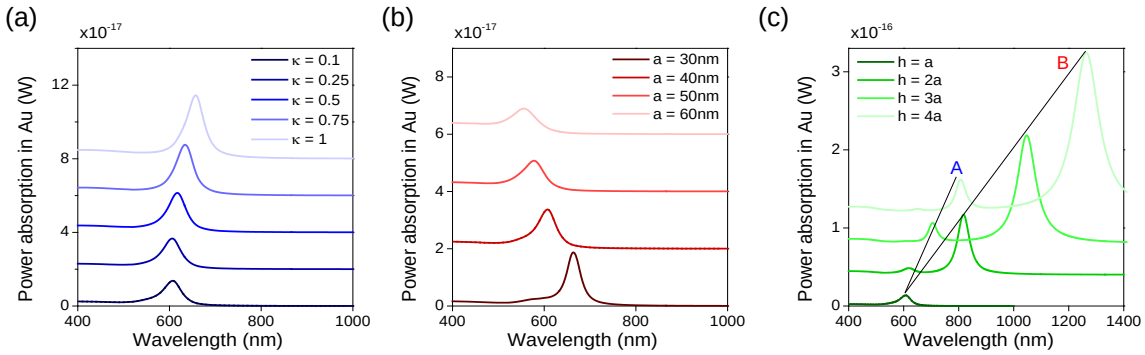

Figure S2: Tunable antenna mode. (a) The spectra of absorption in nanoemitter as a function of aspect ratio κ, with side length $a = 40$ nm and height $h = 40$ nm. (b) The spectra of absorption in nanoemitter as a function of side length a, with aspect ratio $\kappa = 0.1$ and height $h = 40$ nm. (c) The spectra of absorption in nanoemitter as a function of height h, with side length $a = 40$ nm and aspect ratio $\kappa = 0.1$. In all cases, the dielectric coating has thickness of $d = 1$ nm and refractive index of $n = 1.5$.

S3. Effects of Coating on Antenna Mode

The ultrathin dielectric coatings are capable of enhancing the electric fields *via*: (i) plasmonic field confinement following the boundary conditions at the dielectric-vacuum interface; (ii) high refractive index contributing to strong light coupling effect in terms of improving the light absorption efficiency. However, for different configurations that support different modes, *e.g.*, antenna mode in nanopyramid-on-mirror and bonding dipole plasmon (BDP) mode in nanosphere dimer, they have distinct effects on the field enhancement profiles.

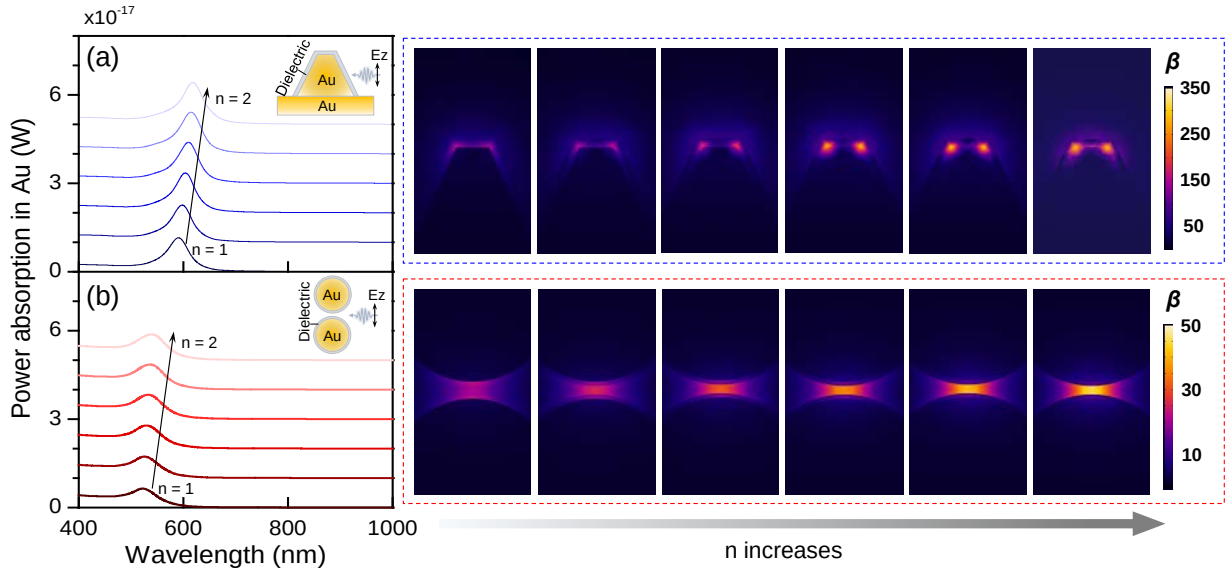

Figure S3: Effect of coatings. The absorption spectra and the cross-sectional views on the field enhancement profiles as a function of coating refractive index n for (a) nanopyramid-on-mirror supporting antenna mode, and (b) nanosphere dimer in vacuum supporting bonding dipole plasmon (BDP) mode. In all cases, the dielectric coatings have a thickness of $d = 1$ nm. The nanopyramid has geometrical parameters of side length $a = 40$ nm, aspect ratio $\kappa = 0.1$, and height $h = 40$ nm. The nanosphere dimer has sphere diameter of 40 nm, and shell-to-shell gap of 2 nm.

We study and compare the effects of the coatings on the antenna mode in a nanopyramid-on-mirror (side length $a = 40$ nm, aspect ratio $\kappa = 0.1$, and height $h = 40$ nm) and the BDP mode in a nanosphere dimer (sphere diameter of 40 nm and shell-to-shell gap of 2 nm) by varying the refractive index from $n = 1$ to $n = 2$ of a 1nm-thick coating in Fig. S3. Firstly, for both configurations, the plasmon resonance, identified at the peak of the absorption spectra, red-shifts as the coating index n increases. Meanwhile, the magnitude of the peak also increases, suggesting

a stronger light coupling manifested by an increased light absorption efficiency.

Secondly, the more prominent effect is the field enhancement profiles of antenna mode and BDP mode. For BDP mode, the maximum field enhancement occurs at the center of the dimer gap.[1] As the coating index n increases, the field is squeezed tighter and tighter inside the air gap, resulting in an increased field enhancement. In contrast, for antenna mode, the maximum field enhancement always occurs at the metal surface. As the coating index n increases, the field is even more closely confined to the metal surface, accompanied with an increased field enhancement.

S4. Validation of Triangular-Barrier-Approximation

We compare our quantum photoemission model based on triangular-barrier-approximation with a modified Fowler-Nordheim rate equation developed for oxidized emitters with a double-barrier.[2,3] In accordance with the scenario of the coated Au tip, the modified Fowler-Nordheim rate equation is generalized as:

$$J(t) = H\left[F(t)\right] \frac{e^3 F_{\mathrm{die}}^2(t)}{16\pi^2 \hbar W B^2} \exp\left[-\frac{4\sqrt{2m}}{3e\hbar F_{\mathrm{die}}(t)} W^{3/2} C\right], \tag{S1}$$

with

$$B = \sqrt{\frac{W_{\mathrm{eff}}}{W}} - H\left[W_{\mathrm{eff}} - eF_{\mathrm{die}}(t)d\right] \sqrt{\frac{W_{\mathrm{eff}} - eF_{\mathrm{die}}(t)d}{W}} + H\left[W - eF_{\mathrm{die}}(t)d\right] \frac{1}{\varepsilon_{\mathrm{die}}} \sqrt{\frac{W - eF_{\mathrm{die}}(t)d}{W}}, \tag{S2}$$

and

$$C = \left(\frac{W_{\mathrm{eff}}}{W}\right)^{3/2} - H\left[W_{\mathrm{eff}} - eF_{\mathrm{die}}(t)d\right] \left[\frac{W_{\mathrm{eff}} - eF_{\mathrm{die}}(t)d}{W}\right]^{3/2} + H\left[W - eF_{\mathrm{die}}(t)d\right] \frac{1}{\varepsilon_{\mathrm{die}}} \left[\frac{W - eF_{\mathrm{die}}(t)d}{W}\right]^{3/2}, \tag{S3}$$

where e and m are the elementary charge (> 0) and electron mass respectively, $\hbar$ is the reduced Planck constant, W is the work function of Au, $W_{\mathrm{eff}} = W - \chi$ is the effective work function at metal-dielectric interface, d is the thickness of the dielectric, $\varepsilon_{\mathrm{die}} = n^2$ is the relative permittivity of the dielectric with refractive index n, $H(x)$ is the Heaviside function, F_{die} is the effective laser field strength inside the dielectric. Here, $F_{\mathrm{die}} = \beta_{\mathrm{Au}} F$ is taken as the field at the metal-dielectric interface from the full-wave simulations, where F represents the field strength of the incident laser. In case of no coating layer, $W_{\mathrm{eff}} = W$, $d = 0$, $\varepsilon_{\mathrm{die}} = 1$, B and C become 1, and Eq. (S1) recovers to the Fowler-Nordheim equation. To compare with our quantum photoemission model, the time-dependent emission current density calculated from Eq. (S1) is averaged over a period of the laser field of angular frequency ω:

$$J = \frac{\omega}{2\pi} \int_0^{2\pi/\omega} J(t)dt. \tag{S4}$$

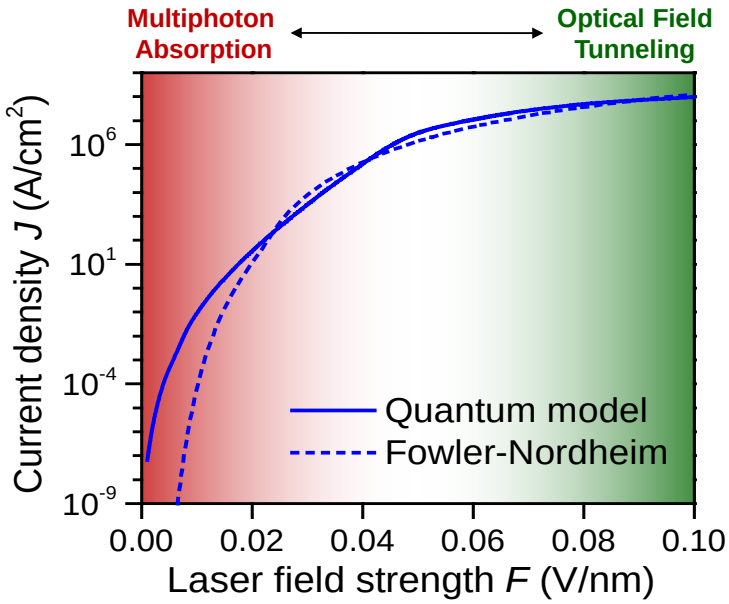

Figure S4: Validation of triangular-barrier-approximation. The emission current density J for the coated emitter, calculated from the quantum photoemission model in the main text (solid line, identical to Fig. 2c), and the modified Fowler-Nordheim rate equation[2,3] (dash line), as a function of incident laser field strength F. The dielectric coating has $d = 1$ nm, $n = 1.5$, and $\chi = 0.9$ eV.

The emission current density J, calculated from our quantum photoemission model and the modified Fowler-Nordheim rate equation for the coated Au emitter is shown in Fig. S4 as a function of the field strength of the incident laser F. The emission current density calculated from those two models shows *quantitatively* good agreement for larger F when approaching the optical field tunneling regime. For smaller F where multiphoton absorption becomes the dominant emission mechanism, the Fowler-Nordheim rate equation significantly underestimates the emission current density, since it is valid only in the strong-field approximation[3] and is no longer applicable in the multiphoton absorption regime.

References

(1) Zhai, Y.; Deng, L.; Chen, Y.; Wang, N.; Huang, Y. Reducing the Loss of Electric Field Enhancement for Plasmonic Core–Shell Nanoparticle Dimers by High Refractive Index Dielectric Coating. *J. Phys. Condens. Matter.* **2019**, *32*, 105001.

(2) Huang, Q.-A. Instability of Field Emission from Silicon Covered with a Thin Oxide Due to Electron Trapping. *J. Appl. Phys.* **1996**, *79*, 3703–3707.

(3) Keathley, P. D.; Sell, A.; Putnam, W. P.; Guerrera, S.; Velásquez-García, L.; Kärtner, F. X. Strong-Field Photoemission from Silicon Field Emitter Arrays. *Ann. Phys. (Berlin)* **2013**, *525*, 144–150.